Microporous Multiresonant Plasmonic Meshes by Hierarchical Micro–Nanoimprinting for Bio-Interfaced SERS Imaging and Nonlinear Nano-Optics

*Aditya Garg, Elieser Mejia, Wonil Nam, Meitong Nie, Wei Wang, Peter Vikesland, and Wei Zhou**

Microporous mesh plasmonic devices have the potential to combine the biocompatibility of microporous polymeric meshes with the capabilities of plasmonic nanostructures to enhance nanoscale light–matter interactions for bio-interfaced optical sensing and actuation. However, scalable integration of dense and uniformly structured plasmonic hotspot arrays with microporous polymeric meshes remains challenging due to the processing incompatibility of conventional nanofabrication methods with flexible microporous substrates. Here, scalable nanofabrication of microporous multiresonant plasmonic meshes (MMPMs) is achieved via a hierarchical micro-/nanoimprint lithography approach using dissolvable polymeric templates. It is demonstrated that MMPMs can serve as broadband nonlinear nanoplasmonic devices to generate second-harmonic generation, third-harmonic generation, and upconversion photoluminescence signals with multiresonant plasmonic enhancement under fs pulse excitation. Moreover, MMPMs are employed and explored as bio-interfaced surface-enhanced Raman spectroscopy mesh sensors to enable in situ spatiotemporal molecular profiling of bacterial biofilm activity. Microporous mesh plasmonic devices open exciting avenues for bio-interfaced optical sensing and actuation applications, such as inflammation-free epidermal sensors in conformal contact with skin, combined tissue-engineering and biosensing scaffolds for in vitro 3D cell culture models, and minimally invasive implantable probes for long-term disease diagnostics and therapeutics.

1. Introduction

Due to their low elastic moduli and high permeability to nutrients and oxygen, mesh-like flexible microporous devices confer significant biocompatibility advantages to interface with cell networks and tissues for biomedical sensing or actuation applications.[1] Most microporous mesh devices employ arrays of electrical components, including microelectrodes[2] and nanoscale transistors.[3] Such electrical mesh devices can serve as inflammation-free epidermal sensors for long-term health monitoring,[4] sensor-array scaffolds for in vitro drug-response monitoring in 3D cell culture models,[5] and minimally invasive brain probes for in vivo electrical recording in animals.[6,7] Despite the benefits of the wireless optical operation, there is little work to date on optical mesh devices based on dense plasmonic nanoantenna arrays for bio-interfacing applications.

Plasmonic nanoantennas based on metal nanostructures can support surface plasmon resonances to enhance light–matter interactions at the nanoscale for bio-interfaced spectroscopy, sensing, and actuation.[8,9] For example, plasmonic nanoantennas can enable surface-enhanced Raman spectroscopy (SERS) for ultrasensitive detection of biochemical analytes[10] and in situ molecular profiling of living biological systems.[11] Furthermore, plasmonic nanoantennas modified with specific receptors can allow refractive index sensing of target biomolecules in biological environments.[12] Finally, plasmonic nanoantennas can serve as nanolocalized photothermal heat sources to induce cell membrane optoporation for drug delivery[13] and stimulate neuron excitation.[14] Therefore, it is highly desirable to develop microporous mesh plasmonic devices for bio-interfaced optical sensing and actuation applications.

Conventional plasmonic nanoantennas optimize single-resonant optical characteristics within one wavelength band and are sufficient for applications based on single-photon and single-band processes. Nevertheless, for emerging nanophotonics applications involving multiphoton processes, it

A. Garg, E. Mejia, W. Nam, M. Nie, W. Zhou
Department of Electrical and Computer Engineering
Virginia Tech
Blacksburg, VA 24061, USA
E-mail: wzh@vt.edu

W. Wang, P. Vikesland
Department of Civil and Environmental Engineering
Virginia Tech
Blacksburg, VA 24061, USA

The ORCID identification number(s) for the author(s) of this article can be found under https://doi.org/10.1002/smll.202106887.

DOI: 10.1002/smll.202106887

is crucial to use multiresonant plasmonic nanostructures to simultaneously enhance light–matter interactions in several resonant spectral bands.[15–17] For example, multiresonant plasmonic enhancement of multiphoton excitation and emission transitions can boost second harmonic generation (SHG) or upconversion photoluminescence (UCPL) signals for deep-tissue optical sensing and imaging.[8,15,18,19] Moreover, multiresonant plasmonic nanostructures enable wavelength-multiplexed multimodal optical operations at the nano-bio interface.[15,20] A general approach to construct multiresonant plasmonic devices is to assemble multiple building-block plasmonic resonators within a very close distance.[21] The optical coupling between the elementary modes of the building blocks can result in multiple hybridized plasmonic modes with spatial overlaps at different wavelengths.[15] Recently, several multiresonant plasmonic devices have been generated using top-down fabrication methods such as electron-beam lithography,[22] focused ion beam,[23] deep-ultraviolet lithography,[24] laser-direct-writing,[25] and nanoimprint lithography (NIL).[17] Despite significant research efforts, to date, the existing multiresonant plasmonic devices face challenging issues, such as relatively low hotspot density, weak excitability of multipolar modes, and lack of scalable nanofabrication methods compatible with flexible microporous substrates.

In this work, we develop a dissolvable template-based hierarchical micro-/nanoimprinting approach to create large-area microporous multiresonant plasmonic mesh (MMPM) devices for bio-interfacing applications. The MMPMs carry two-tier nanolaminate plasmonic crystals (NLPCs) consisting of two optically coupled nanodome and nanohole multiresonant subsystems. By supporting multiple spatially overlapped plasmonic modes, MMPMs allow multiresonant plasmonic enhancement of SHG, third-harmonic generation (THG), and UCPL emissions under fs laser pulses over a wide excitation wavelength range. Moreover, we demonstrate that MMPMs can support dense and uniform SERS hotspots arrays for in situ spatiotemporal molecular profiling of bacterial biofilm formation and growth.

2. Fabrication of MMPMs

Figure 1A illustrates the fabrication processes used to create the MMPMs. First, thermal micro-/nanoimprint lithography was exploited to replicate water-soluble polyacrylic acid (PAA) micropillar arrays and solvent-soluble polymethyl methacrylate (PMMA) nanowell arrays from hydrophobic perfluoropolyether (PFPE) replica molds (Figure S1, Supporting Information). Then, alternating layers of Au (10 nm) and SiO_2 (8, 10, and 12 nm from top to bottom) were deposited within the PMMA nanowell arrays using electron beam deposition. The metal and dielectric thicknesses were selected to achieve multiresonant plasmonic responses across a broad visible to near-infrared (Vis–NIR) range.[26,27] The cross-sectional scanning electron microscope (SEM) image in Figure 1B depicts NLPCs within the PMMA nanowell arrays. The optical image of NLPCs shows a vivid diffraction pattern, revealing a uniform distribution of periodic nanostructures over a large sample area. Subsequently, a unique hierarchical micro-/nanoimprint lithography process was conducted by squeezing a hydrophobic UV-curable resist (PFPE) between the PAA micropillar arrays and the NLPCs-containing PMMA nanowell arrays under high pressure with UV curing. Due to their wettability difference, the confined hydrophobic resist can experience partial dewetting with the more hydrophilic PAA and PMMA-NLPCs templates, which possess micro/nanogeometries to reduce

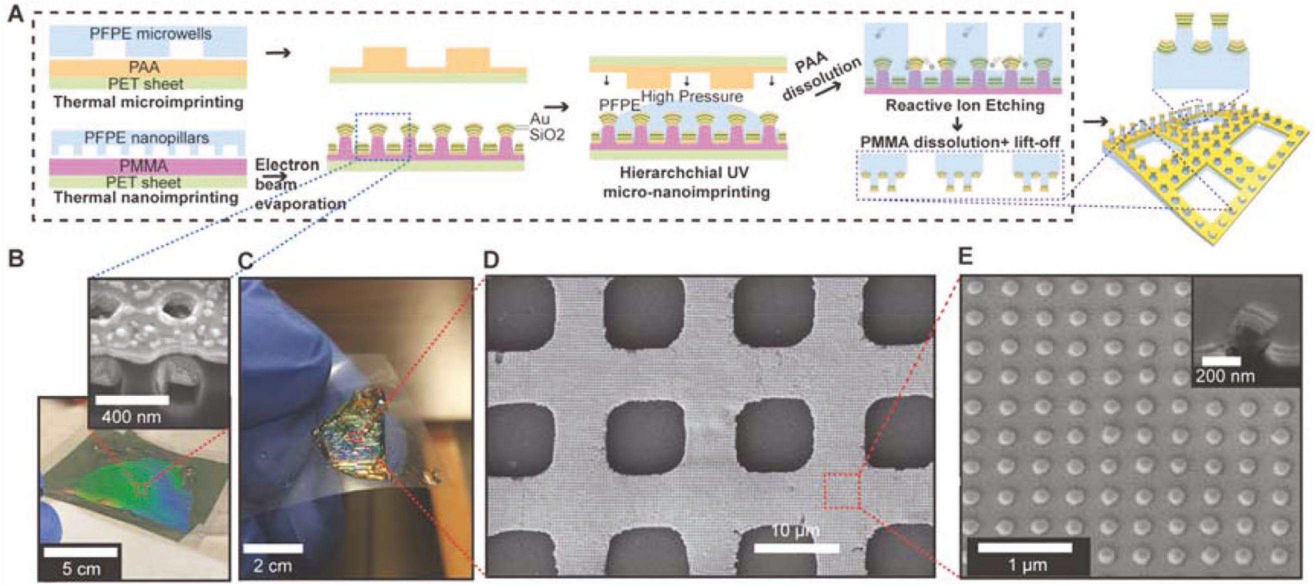

Figure 1. Fabrication of MMPMs using hierarchical micro-/nanoimprint lithography with dissolvable templates. A) Schematic illustration for the fabrication processes. B) Tilted-view bright-field and cross-section SEM images of the PMMA nanohole arrays with NLPCs. C) Tilted-view bright-field image of the MMPM on a PET sheet. D) Top-down SEM image of the MMPM. E) Zoomed-in top-down SEM image and cross-sectional view SEM image of the MMPM depicting the NLPCs.

the thickness of the residual layer further.[28] Then PAA was dissolved in water to expose the microstructured side of the UV-cured PFPE, followed by mild reactive ion etching (RIE) in the plasma of oxygen and CF_4 mixtures to eliminate the thin residual layer. Because PMMA is water-insoluble, the PMMA template remained attached to the UV-cured PFPE, thus keeping the sample flat and robust, allowing uniform RIE etching of the residual layer and facile sample handling. Subsequently, PMMA was dissolved in anisole to lift off the MMPM. Successful transfer of the NLPCs onto the UV-cured PFPE scaffolds with excellent transfer yield was achieved due to the solvent-solubility of the PMMA template, whereby solvent molecules can weaken the adhesion between the NLPCs and PMMA templates to allow the reliable release of the plasmonic nanostructures.[29] Additionally, mechanically stable plasmonic hotspot arrays were generated due to the strong bonding between the UV-cured PFPE scaffold and the NLPCs.[30] Lastly, RIE was performed to expose the plasmonic nanogap hotspots of the NLPCs embedded in the UV-cured resist, followed by partial etching of the SiO_2 layers using buffered oxide etchant (BOE) to open the plasmonic nanogap hotspots.[31] Figure 1C illustrates an oblique-angle optical image of the MMPM, displaying a bright diffraction pattern from the periodic nanostructures on the sample. The top-view SEM image depicts the microporous structure (pore size = 8 µm, periodicity = 16 µm) of the MMPM and the uniform periodicity of the plasmonic nanostructures (Figure 1D,E), while the cross-sectional SEM shows the multilayered metal–insulator–metal (MIM) nanohole and nanodome sub-systems (Figure 1E). The tapered shape of the MIM nanodome arrays is due to the shadowing effect from the line-of-sight electron-beam deposition process. The integration of dense and mechanically stable NLPCs with biomimetic microporous polymeric scaffolds is enabled by our unique fabrication process, which combines several novel aspects: 1) partial dewetting of a hydrophobic, UV curable resist with hydrophilic micro/nanostructured templates to minimize the residual layer thickness during imprinting, 2) solvent-solubility of the nanostructured template enabling the transfer of the NLPCs onto polymeric scaffolds with excellent transfer yield, 3) hierarchical solubility of the micro- and nanostructured templates enabling the uniform and user-friendly RIE etching processing for reproducibly eliminating the polymeric residual layer, 4) strong bonding between the UV-cured polymeric scaffold and the NLPCs generating mechanically stable plasmonic hotspot arrays, and 5) mild processing steps with low-toxicity solvents at low temperature thus allowing manufacturing compatibility with UV-curable polymers. The biomechanical properties (e.g., low bending stiffness comparable with biological systems (Figure S2, Supporting Information)[7] and high permeability to nutrients and oxygen) of the biomimetic polymeric scaffold coupled with the multiresonant plasmonic capabilities of the NLPCs enable active monitoring or actuation of biological activities in living systems with unique biocompatibility benefits.

3. Optical Properties and Multiphoton Nonlinear Responses of the MMPM

We carried out reflectance and transmittance measurements of the sample to demonstrate that the MMPM exhibits a broadband multiresonant response (**Figure 2**A and Figure S3, Supporting Information). As shown in Figure 2A, the measured reflectance spectrum of the MMPM exhibits narrow reflectance dips at 600, 735, and 790 nm and a broad reflectance dip at 1050 nm that covers the wide spectral range from 900 to 1500 nm, indicating a broadband multiresonant response. To further understand the multiple resonance features in the reflectance spectra, we calculated the far-field and near-field optical properties of the MMPM using the finite-difference time-domain (FDTD) method. The FDTD model used for calculations consists of an

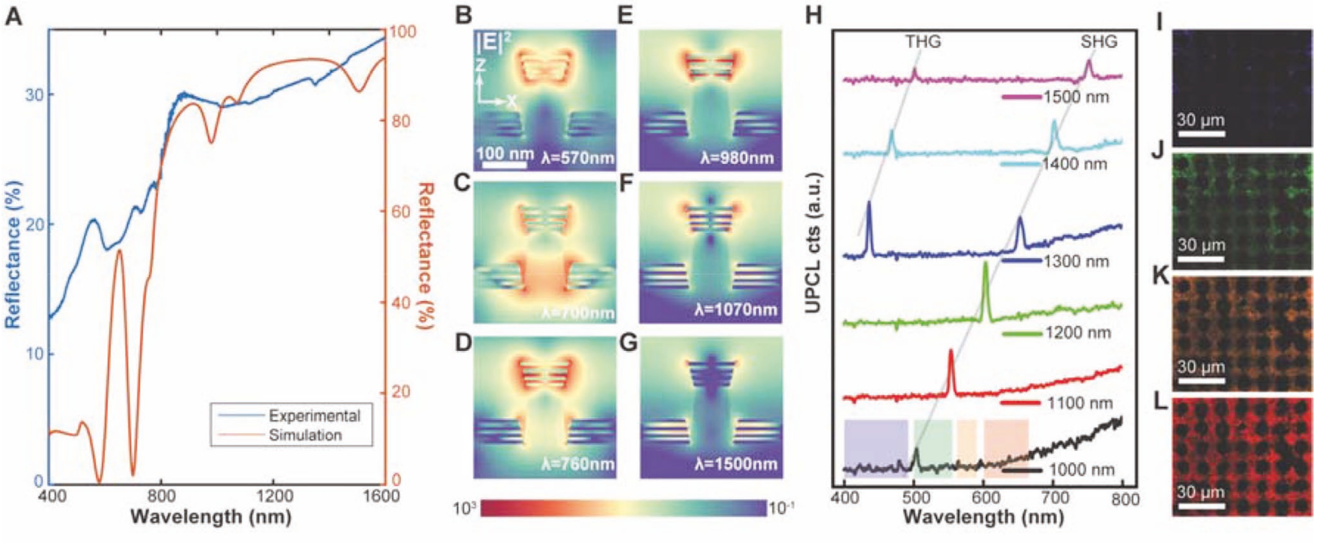

Figure 2. Optical properties and multiphoton nonlinear responses of the MMPM. A) Measured and FDTD-calculated reflectance spectra of the MMPM. B–G) The FDTD-calculated *x*–*z* distribution map of $|E|^2$ for the NLPCs at B) 570 nm, C) 700 nm, D) 760 nm, E) 980 nm, F) 1070 nm, and G) 1500 nm. H) Spectra of nonlinear scattered light under fs-laser excitation in the near-infrared region from 1000 to 1500 nm. I–L) Multiphoton microscopy 2D images under fs-laser excitation at 1000 nm with the emission detected at I) 400–492 nm, J) 500–550 nm, K) 563–588, and L) 601–657 nm.

infinite array of nanolaminate nanoholes and nanodisks and does not account for the microscale pores on the MMPM that facilitate light transmission. Therefore, the overall reflectance amplitude of the FDTD-calculated reflectance spectra is higher than the measured reflectance spectra (Figure 2A). The FDTD-calculated reflectance spectra exhibit six plasmonic resonant dips at 570, 700, 760, 980, 1070, and 1500 nm. Compared to the experimentally measured spectra, the calculated spectra show resonant peaks with narrower linewidths because of inhomogenous broadening effects arising from random geometrical variations between the unit cell structures and homogenous broadening effects from optical losses due to metal–dielectric interface roughness.[32] The geometrical variations between the unit cell structures of the NLPCs can primarily be attributed to the nanoscale structural inhomogeneity of the PMMA nanowell arrays due to the inherent limitations of the NIL process such as template degradation after several imprinting cycles[33] and the inhomogeneity in NLPC unit cells at the edges of the micropores due to the lack of alignment between the microtemplate and nanotemplate. The FDTD calculations (Figure 2B–G) reveal six resonant plasmonic modes with electric field intensity enhancement $>10^3$. The modes at 570 and 980 nm (Figure 2B,E) primarily originate from localized plasmonic modes in the MIM nanodome arrays. The mode at 1500 nm (Figure 2G) mostly derives from the delocalized plasmonic modes in the MIM nanohole arrays. The modes at 700, 760, and 1070 nm (Figure 2C,D,F) originate from optical hybridization between the delocalized plasmonic modes in the MIM nanolaminated nanohole array and localized plasmonic modes in the MIM nanolaminated nanodisk arrays, enabling the enhancement of linear and nonlinear optical processes over a broad wavelength range.[26] Figure 2H shows the nonlinear upconversion light emission spectra between 400 and 800 nm under fs pulses at different excitation wavelengths between 1000 and 1500 nm. The spectra exhibit three main components: THG peaks, SHG peaks, and a broadband UCPL feature.[34,35] Since the MMPM exhibits a broadband multiresonant response in the Vis–NIR region with high local field enhancement (Figure 2A–G), SHG,[36] THG,[37] and UCPL[34] signals are boosted over a broad excitation wavelength range from 1000 to 1500 nm via the enhancement of multiphoton excitation and emission processes (Figure 2H). Indeed, the noncentrosymmetric geometry of the two-tier NLPCs and the symmetry break at the metal–dielectric interfaces can cause SHG signals due to nonvanishing nonlinear surface susceptibility and nonlocal spatial field variation.[18,38] As shown in Figure 2H, under 1000 nm fs-laser excitation, the nonlinear spectra exhibit a strong UCPL peak covering a broad spectral range from 550 to 880 nm and a weak SHG peak at 500 nm. Under this excitation condition, the multiphoton excitation of electron–hole pairs in the sp-band of gold can result in UCPL.[34,35] Since a large portion of the incident energy is converted to multiphoton UCPL, the coherent SHG signals are weaker under 1000 nm excitation.[39] As the excitation wavelength increases from 1000 to 1100 and 1200 nm, the UCPL signal gets weaker, and the SHG signals become stronger. As the excitation wavelength increases from 1200 to 1500 nm, the intensity of the SHG peak gradually decreases. In addition, THG peaks can also be observed within the spectral range of the detection system under fs-laser excitation from 1300 to 1500 nm, and the intensity of the THG peaks decreases as the excitation wavelength increases. This decreased intensity of the SHG and THG peaks can be attributed to the weaker plasmonic enhancement at excitation and/or emission wavelengths by the MMPM as indicated by the measured reflectance spectra (Figure 2A). However, further investigation is required to fully understand the contributions of the spatially overlapped plasmonic modes at the excitation and emission wavelengths to the nonlinear signal enhancement. Figure 2I–L shows multiphoton microscopy 2D images of the MMPM with the excitation using a 1000 nm fs laser and the emission simultaneously detected in four spectral channels (channel 1: 400–492 nm, channel 2: 500–550 nm, channel 3: 563–588 nm, and channel 4: 601–657 nm). As expected, no signal was detectable in channel 1 due to the absence of multiphoton emission processes (Figure 2I). However, strong signals were detected in channel 2, which can be attributed to SHG (Figure 2J). In addition, strong signals were also detected in channels 3 and 4 due to the multiphoton UCPL (Figure 2K,L). These results manifest that the multiresonant plasmonic meshes can potentially enable deep-tissue optical sensing and imaging at the nano-biointerface via plasmonic enhancement of multiphoton excitation and emission processes.

4. SERS Performance of the MMPM

We coated the NLPCs with a self-assembled monolayer of benzenethiol (BZT) molecules, a nonresonant Raman probe, to evaluate SERS performance under 785 nm laser excitation. Before BZT monolayer formation, RIE was performed to expose the SERS hotspots embedded in the UV-cured resist via a combination of physical bombardment and chemical reaction followed by the partial etching of the SiO_2 layers using BOE to open the plasmonic nanogap hotspots of the NLPCs and improve their accessibility to the analyte (Figure S4A, Supporting Information). The optimized RIE etching time of 1 min exhibited high SERS sensitivity (SERS EF = 4.8×10^6) and excellent uniformity (RSD = 9.0%) over a large area by exposing the embedded SERS hotspots while minimizing the structural deformation of the NLPCs that result from RIE undercutting of the polymer matrix supporting the NLPCs (Figure S4B,C, Supporting Information). To evaluate the backside excitability of the multiresonant plasmonic mesh, we acquired SERS signals from both the front and back sides of the MMPM. The SERS spectra of BZT evaluated under backside excitation demonstrate a comparable SERS signal intensity (≈85%) relative to those acquired using excitation from the front side (**Figure 3**A,B). Histograms of the 1077 cm^{-1} BZT Raman peak intensities and the corresponding SERS EFs from 75 pixels display a normal distribution profile under excitation from both front and back sides, revealing a uniform SERS hotspot distribution (Figure 3B).[40] Figure 3C illustrates the 2D Raman mapping at 1077 cm^{-1} over a 100 µm × 100 µm area containing 10 000 pixels, along with the corresponding bright-field image. No BZT Raman signals were observed on the right side of the 2D Raman map as the ultra-flexible MMPM was bent out-of-focus in that region, as indicated by the bright-field

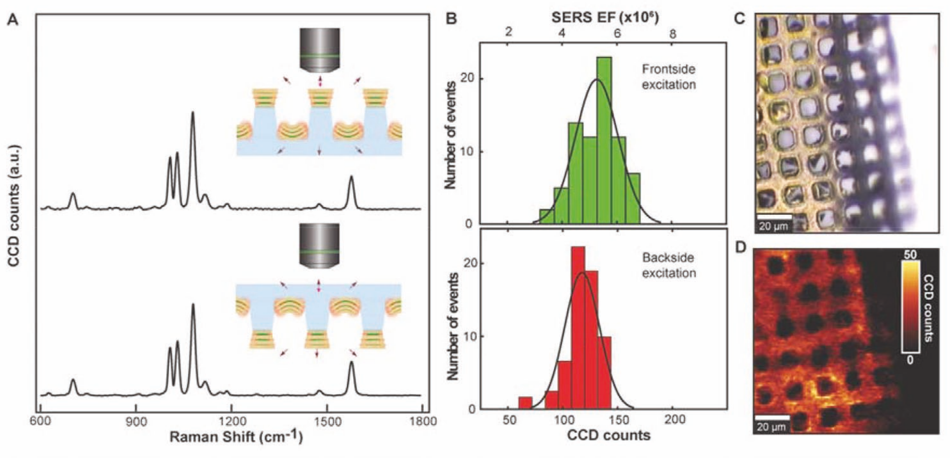

Figure 3. SERS performance of the MMPM. A) The measured Raman spectra of BZT molecules self-assembled on the surface of the NLPCs under 785 nm laser excitation from the front and back sides. B) Histograms of Raman signal intensities and the corresponding SERS EFs (1077 cm^{-1}) from 75 pixels over three different regions (5 μm by 5 μm each) of the MMPM under the frontside and backside laser excitation. C) Bright-field images and D) the corresponding scanning confocal Raman images (1077 cm^{-1}) of the MMPM.

image (Figure 3C). However, the uniform signal intensities observed in the in-focus regions of the 2D Raman image validate the highly uniform distribution of SERS hotspots over large areas of the microporous polymeric scaffold.

5. In Situ Spatiotemporal Molecular Profiling of Bacterial Biofilm Formation and Growth Processes

The MMPMs combine the biomechanical compatibility and transport permeability of microporous ultrathin polymeric meshes with the Raman fingerprint specificity, plasmonic sensitivity, and structural uniformity of NLPC hotspot arrays. Therefore, the MMPMs can serve as bio-interfaced mesh SERS sensors for in situ spatiotemporal biochemical monitoring of biological systems. To demonstrate the ability of the MMPM for in situ spatiotemporal biochemical monitoring of biological systems, we exploited the MMPM coupled with a transparent bandage to continuously monitor bacterial biofilms on LB agar plates. As shown in **Figure 4**A,B, the MMPM bandage can seamlessly interface with *Pseudomonas syringae* bacterial colonies on an LB agar layer. Bacterial colony proliferation was observed on the LB agar plates under the MMPM bandage (Figure S5, Supporting Information), and the molecular signatures reflecting the biofilm formation process were continuously monitored for 48 h via SERS measurements under the backside excitation. Figure 4C illustrates the temporal variability of the average SERS spectra between 0 and 48 h, with Table S1 in the Supporting Information providing assignments and origins for the observed SERS peaks. Spatiotemporal SERS measurements were obtained for 5×5 pixels over a 25 μm^2 region under 785 nm laser excitation. We calibrated SERS signal intensities with the electronic Raman scattering (ERS) internal standard for Raman peaks across different measurements.[41] Briefly, the control SERS spectrum measured from LB broth exhibits major bands at 732 and 1002 cm^{-1} that reflect constituent purines (adenine) and proteins (phenylalanine). For *P. syringae* colonies after seeding at $t = 0$ h, the measured SERS spectrum shows reduced peak intensities at 732 and 1001 cm^{-1} related to LB broth components and a new lipid peak at 1444 cm^{-1}, possibly originating from the lipid outer membrane of the cells,[42] manifesting an intimate interface of SERS hotspots with *P. syringae* cells to probe membrane components but with reduced access to LB broth components.[43] At $t = 6$ h, a nucleic acid peak at 968 cm^{-1} emerges, possibly originating from extracellular DNA (eDNA) that promotes surface attachment and cell–cell adhesion during the early stages of biofilm formation.[44,45] As the biofilm develops from 6 to 48 h, the peak for nucleic acids (968 cm^{-1}) decreases in intensity, while several peaks associated with biofilm extracellular polymeric substance (EPS)[46] proteins (638, 822, 1180, 1240, 1366), carbohydrates (858 and 1140 cm^{-1}), and lipids (1305 and 1444 cm^{-1}) emerge.[47,48] These observations reflect that mesh SERS hotspot arrays experience increased exposure to EPS components (e.g., polysaccharides and proteins) and reduced exposure to the cell membrane and eDNA components during the biofilm formation and growth process. In this scenario, the increasing depth of the EPS layer within the biofilm may limit access of the buried cells and eDNA components to the SERS hotspots in the mesh sensors.[45,49] Figure 4D illustrates the time-dependent in situ SERS maps for major Raman bands during biofilm formation. Despite the uniformity of the hotspot arrays in the mesh SERS biosensors, spatiotemporal maps of different Raman bands show dynamic changes and nonuniform distributions, thus reflecting the complex spatiotemporal evolution of network-level microbial activity during biofilm growth. For quantitative analysis of temporal biochemical changes during the biofilm growth process, the ERS-calibrated Raman intensity of major peaks from proteins, carbohydrates, lipids, and nucleic acids was plotted as a function of time (Figure 4E and Figure S6, Supporting Information). First, we observe that the intensities of the peaks from LB medium components (732 and 1001 cm^{-1}) continually decrease as the biofilm develops from 6 to 48 h, indicating the consumption of LB medium components by *P. syringae*

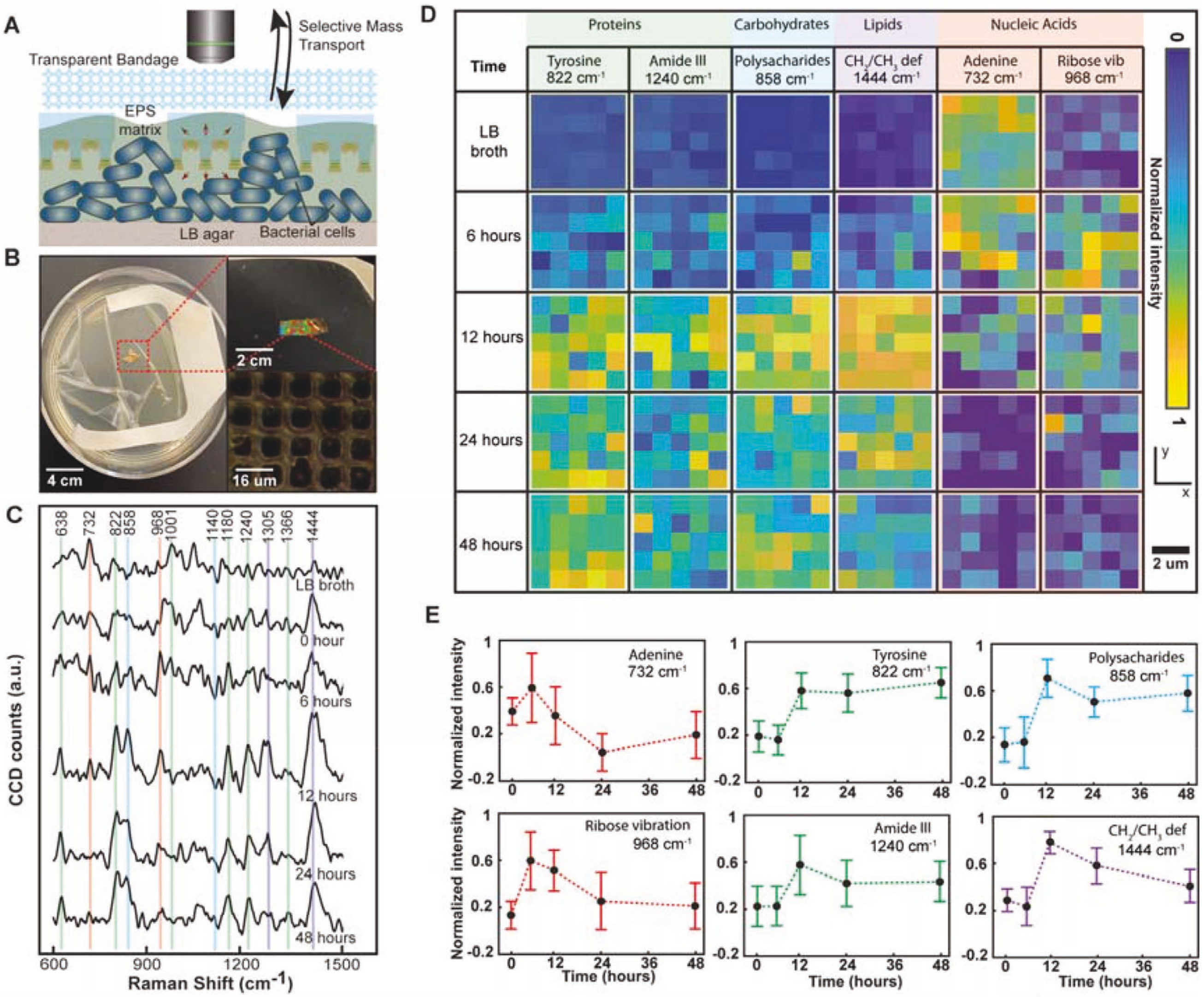

Figure 4. In situ spatiotemporal molecular profiling of bacterial biofilm formation and growth. A) Schematic illustration of the experimental setup. B) Top-down image of the MMPM bandage interfaced with *Pseudomonas syringae* bacterial colonies on an LB agar plate, zoomed-in tilted view image of the MMPM bandage, and top-down bright-field image of the MMPM bandage. C) Average SERS spectra of *Pseudomonas syringae* biofilms measured between 0 and 48 h (green bars = protein peaks, red bars = nucleic acid peaks, blue bars = carbohydrate peaks, and purple bars = lipid peaks). D) 2D Raman images for *Pseudomonas syringae* biofilms measured between 6 and 48 h at 732, 822, 858, 964, 1240, and 1444 cm^{-1}. E) The ERS-calibrated Raman intensities for *Pseudomonas syringae* biofilms measured between 0 and 48 h at 732, 822, 858, 964, 1240, and 1444 cm^{-1}.

(Figure 4E). Second, we observe that some peaks from proteins (822 and 1366 cm^{-1}) and carbohydrates (1040 cm^{-1}) continually increase in intensity as the biofilm grows from 6 to 48 h, while other peaks (858 and 1240 cm^{-1}) initially increase (6 to 12 h) and then saturate (12–48 h). Previous studies have shown that proteins and carbohydrates, major EPS components, increase significantly during the biofilm development process.[47] Lastly, we observe that the peaks from lipids (1305 and 1440 cm^{-1}) and nucleic acids (668 cm^{-1}) initially increase in intensity and subsequently decrease in intensity between 12 and 48 h. This reduced intensity at later stages of biofilm development is attributed to the reduced exposure of the embedded cell wall and eDNA components to the SERS hotspots.

6. Multivariate SERS Analysis and Classification of Bacterial Biofilm Growth Stages

We employed multivariate chemometric methods to further analyze the complex multivariable spectroscopic data originating from molecular ensembles in the plasmonic hotspots. In this work, principal component analysis (PCA) and linear discriminant analysis (LDA) were hierarchically implemented to analyze and classify the Raman data from the different biofilm growth stages. PCA reduces the dimensionality of multivariable datasets while preserving the variance of the datasets. The loading plots of the principal components (PCs) can then be used to identify the significant spectral components from the spectroscopic data, and the PC score scatter plots can be

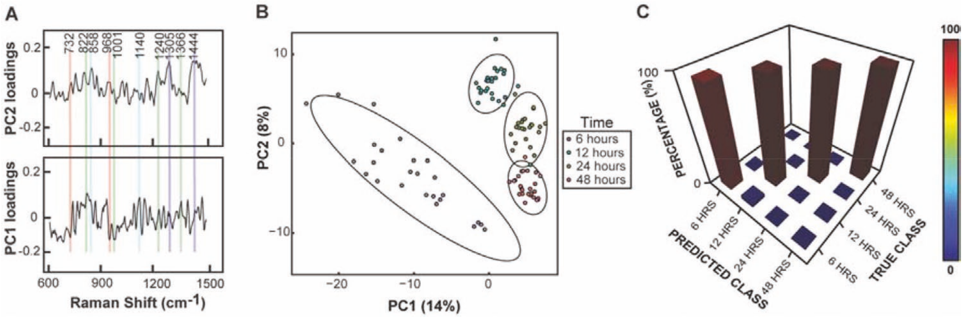

Figure 5. Multivariate SERS analysis and classification of bacterial biofilm growth stages: A) PC1 and PC2 loading plots and B) PC score scatter plot of *Pseudomonas syringae* biofilm growth stages. C) Histograms of a confusion matrix for PCA-LDA with LOOCV.

used to visualize the statistical segregation between different data classes. **Figure 5**A shows loading plots of the first principal component (PC1) and the second principal component (PC2), exhibiting significant contributions to the loadings from several spectral components. The PC1 loading plot shows that the spectral features arising from the LB medium components (e.g., 732 and 1001 cm^{-1}) and nucleic acids (e.g., 968 cm^{-1}) negatively contributed to the PC1 loadings, while several spectral features from proteins (e.g., 822 and 1366 cm^{-1}) and carbohydrates (858 and 1140 cm^{-1}) positively contributed to the PC1 loadings. In addition, the PC2 loading plot shows that the spectral features assigned to lipids (e.g., 1305 and 1444 cm^{-1}) strongly contributed to the PC2 loadings positively. Although the origins of several significant spectral features identified by the PC loadings could be assigned based on previous studies (Table S1, Supporting Information), the assignment of other unknown spectral components identified by the PC loadings requires further analysis using analytical methods such as mass spectrometry. Figure 5B shows a PC score scatter plot from different stages of the biofilm development process from 6 to 48 h, showing the slight overlap between the biofilm measured at 24 and 48 h. Although the first two PC loadings show significant contributions from nucleic acid-, protein-, carbohydrate-, and lipid-related peaks (Figure 5A), these two PCs with a 22% contribution are inadequate to separate the multiclass and inhomogenous dataset. PCA is used as a dimensionality reduction tool as it does not account for interclass variability.[50,51] Subsequently, LDA, which can maximize inter-class variance and minimize intraclass variance, was implemented to classify the multivariable dataset, taking the first 25 PCs (80% spectral variance) as the input variables.[50] The leave-one-out-cross-validation (LOOCV) method was implemented to evaluate the predictive capability of the PCA-LDA model, and the classification results indicate that overall accuracy of 99% can be achieved using our PCA-LDA model (Figure 5C and Table S2, Supporting Information).

7. Conclusion

For the first time, we have created microporous multiresonant plasmonic meshes consisting of dense, uniformly structured, and mechanically stable multiresonant plasmonic hotspot arrays on polymeric meshes for bio-interfaced SERS monitoring applications. We report a hierarchical micro-/nanoimprint lithography fabrication process using dissolvable polymeric templates to produce scalable plasmonic meshes, which features several enabling novelties: 1) partial dewetting of UV-curable resists can minimize the thickness of the residual layer during imprinting, 2) solvent-solubility of nanotemplates can allow the transfer of plasmonic nanostructures onto polymeric scaffolds with excellent transfer yield, 3) hierarchical-solubility of micro-/nanotemplates can enable the reproducible elimination of the remaining residual layer for generating microporous scaffolds, and 4) strong adhesion between the UV-cured polymeric scaffold and plasmonic nanostructures can generate mechanically stable plasmonic hotspot arrays. We demonstrate that MMPMs can serve as broadband nonlinear nanoplasmonic devices to generate SHG, THG, and UCPL upconversion signals under fs pulse excitation, opening exciting avenues for bio-interfaced nonlinear optical sensing and imaging applications. We also show that MMPMs can function as bio-interfaced SERS mesh sensors for in situ spatiotemporal SERS molecular profiling of bacterial biofilm activities. We envision that the biomechanical compatibility and transport permeability of microporous ultrathin polymeric meshes coupled with the multiresonant plasmonic capabilities of the NLPC hotspot arrays in the MMPMs can potentially open the door for various bio-interfaced optical sensing and actuation applications such as inflammation-free epidermal sensors in conformal contact with skin, combined tissue-engineering and biosensing scaffolds for in vitro 3D cell culture models, and minimally invasive implantable probes for long-term disease diagnostics and therapeutics.

8. Experimental Section

Fabrication of PAA Microtemplates: 2D arrays of micropillars (periodicity: 16 µm, diameter: 8 µm, height: 1 µm) composed of a negative-tone photoresist (SU8-2000.5, Kayaku Advanced Materials Inc., USA) were generated on silicon substrates via conventional photolithography. PFPE (Fluorolink PFPE, Solvay, Belgium) was used to replicate microwell arrays from the SU-8 mold on a PET sheet using UV nanoimprint lithography (Compact Nanoimprint v2.0, NIL Technology, Denmark). PFPE was squeezed between the mold and PET sheet and cured by UV for 3 min under 2 bar pressure. Next, another round of UV curing for 3 min under vacuum and post-annealing at 100 °C for 45 min was conducted. A 50% w/w solution of PAA (average molecular weight = 1800, Sigma Aldrich, USA) in methanol was prepared and subsequently spin-coated on a PET sheet (3000 rpm, 30 s). Lastly, PAA micropillar arrays were replicated on the PET sheet from the PFPE mold via thermal microimprint lithography. The imprint time, pressure, and temperature were 3 min, 6 bar, and 120 °C, respectively.

Fabrication of PMMA Nanotemplates: A PFPE mold was replicated from a silicon master consisting of a 2D square periodic array of nanowells (periodicity: 400 nm, diameter: 120 nm, height: 300 nm) using UV nanoimprint lithography. UV curing was performed for 3 min under 2 bar pressure, followed by another round of UV curing for 3 min under vacuum and post-annealing at 100 °C for 45 min. A 20% w/w solution of PMMA (average molecular weight = 15 000, Sigma Aldrich, USA) in anisole was prepared and subsequently spin-coated on a PET sheet (3000 rpm, 30 s), followed by heating at 150 °C for 3 min to evaporate the solvent. PMMA nanowell arrays were replicated on the PET sheet from the PFPE mold via thermal nanoimprint lithography. The imprint time, pressure, and temperature were 10 min, 6 bar, and 170 °C, respectively.

Fabrication of MMPMs: Alternating layers of Au (10 nm) and SiO_2 (12, 10, and 8 nm from bottom) were deposited on the PMMA nanowell arrays using e-beam evaporation (PVD250, Kurt J. Lesker, USA). In addition, 0.7 nm of titanium was deposited between the Au and SiO_2 layers for adhesion. Then, PFPE was squeezed between the PAA microtemplate and the NLPC containing PMMA nanotemplate, and cured by UV for 3 min under 6 bar pressure, followed by another round of UV curing for 3 min under vacuum. Then, the system was submerged in water at 70 °C till most of the PAA was dissolved and the PAA microtemplate was released from the UV-cured PFPE. Subsequently, the residual PFPE layer was etched using reactive ion etching (RIE-1C, Samco, Japan) in the plasma of O_2 (5 sccm) and CF_4 (25 sccm) mixtures under the RF power of 50 W for 2 min. Then, the system was placed in anisole at 70 °C to dissolve the PMMA and release the MMPM from the PET substrate. The MMPM was transferred to a beaker of water using a Pasteur pipette and rinsed three times. Subsequently, the rinsed MMPM was transferred to a beaker of ethanol and captured on a PET sheet for post-processing. RIE was performed in the plasma of O_2 (5 sccm) and CF_4 (25 sccm) mixtures under the RF power of 30 W to expose the embedded SERS hotspots. To open the dielectric nanogaps, BOE 10:1 was used (Transene Inc., USA).

Reflectance and Transmittance Measurements: The reflectance and transmittance spectra were measured by a UV-vis–NIR spectrophotometer (Cary 5000, Agilent, USA). The absorption spectra were calculated using the formula (Absorption = 100% − Transmission − Reflection).

FDTD Simulation: A uniform 3 nm mesh was used in *x*-, *y*-, and *z*-directions. The optical constants of Au were taken from Johnson and Christy. The Bloch boundary condition was used in *x*- and *y*-directions with a periodicity of 400 nm, and the perfectly matched layer boundary condition was used in the *z*-direction. The refractive indices of SiO_2 and PFPE were set as 1.50 and 1.34, respectively.

Multiphoton Nonlinear Spectra: The tunable fs laser pulses were generated by using a Ti:sapphire oscillator (Coherent, Chameleon Ultra II) and an optical parametric oscillator (Coherent, Chameleon Compact OPO) with 200 fs pulse duration and 80 MHz repetition rate. The laser pulses were first filtered through two 900 nm longpass filters (Thorlabs, FEL0900) before being introduced into an inverted microscope (Nikon, TE2000-U). The sample was excited under a focused laser beam through a 20x objective (Nikon, NA = 0.4). The nonlinear upconversion signals were collected in the backward direction, filtered by two 900 nm shortpass filters (Edmund Optics, 900SP OD4) and one 850 nm shortpass filter (Edmund Optics, 850SP OD2) to remove the reflected excitation laser, and then directed into a CCD spectrograph (Andor, Kymera 328i/iDus 420) by a multimode optical fiber (Ocean Insight, QP400-2-SR). The excitation laser wavelength was scanned from 1000 to 1500 nm with 100 nm increments. The pump power of the excitation laser at all wavelengths was set to 19 mW. The spectra were acquired for 10 min with two accumulations, with no observable change between each acquisition

Multiphoton Nonlinear 2D Images: The 2D images were acquired using a four-channel multi-photon laser scanning fluorescence microscope (Nikon, A1R-MP) equipped with an ultrafast laser (Coherent, Chameleon Discovery). Fs-laser excitation was performed at 1000 nm with the emission detected at 1) 400–492 nm, 2) 500–550 nm, 3) 563–588, and 4) 601–657 nm.

BZT Raman Measurements: Samples were incubated in 1×10^{-3} m of BZT ethanolic solution for 24 h to generate a self-assembled monolayer. For Raman measurements, a confocal Raman microscope (alpha 300 RSA+, WItec, Germany) equipped with a 785 nm diode laser (Xtra II, Toptica, Germany) was used. The backscattered photons were detected with a spectrometer (UHTS300, WItec, Germany) equipped with a CCD camera (DU401A, Oxford Instruments, UK). Signals were collected via a 20× objective lens with 0.4 mW and 0.1 s integration time. After the signal acquisition, the cosmic rays removal and baseline correction using the Project v4.1 Software (WITec, Germany) were conducted.

SERS EF Calculation: The SERS EF was calculated using the equation EF = $(I_{SERS}/I_{Raman}) \times (N_{Raman}/N_{SERS})$, where I_{SERS}, I_{Raman}, $N_{SERS,}$ and N_{Raman} are the measured SERS intensity, the neat BZT Raman intensity, and the number of BZT molecules contributing to SERS and neat Raman intensity, respectively. For calculating I_{Raman}, the 1094 cm^{-1} peak originating from the C—C—C ring in-plane breathing mode with C—S stretching mode was used. The associated SERS peak at 1077 cm^{-1} was used for calculating $I_{SERS.}$ N_{SERS} was calculated using the equation $N_{SERS} = SA \times \rho_{SERS}$, where SA is the surface area of the SERS substrates under the focused illumination contributing to the enhancement of Raman signal and ρ_{SERS} is the packing density of BZT on Au surface (6.8×10^{14} molecules cm^{-2}). N_{Raman} was calculated using the equation $N_{Raman} = A \times d_{eff} \times \rho_{BZT}$, where *A* is the area of the focused illumination, d_{eff} is an effective focus depth of laser beam spot in the neat BZT solution, and ρ_{BZT} is the density of BZT molecules in the neat solution (5.9×10^{21} molecules cm^{-3}). The d_{eff} was measured by recording the Raman intensity value of Si (527 cm^{-1}) at varying distances between the objective lens and a bare silicon wafer.

Preparation of MMPM Bandages: A drop of ethanol was placed on the MMPM captured on a PET sheet, and the MMPM was allowed to gently slide onto a transparent bandage (Nexcare Tegaderm transparent dressing, 3M, St Paul, MN).

Bacterial Cell Culture: Bacterial strain *P. syringae* was grown from stock on LB agar plates at 25 °C for 48 h. A single colony was transferred to 15 mL of LB medium and incubated at 25 °C with agitation at 200 rpm for 24 h. The bacterial culture (100 µL) was washed three times by centrifugation (4000*g*/8 min) with 10 mL of LB and re-suspended in 10 mL of fresh LB medium. To obtain the bacterial concentration, the obtained bacterial suspensions were diluted in series and placed onto LB agar plates. The colony-forming units (CFUs) were counted after 48 h to obtain the concentration.

SERS Detection of Bacterial Biofilm Formation and Growth Processes: 10 µL of the bacterial suspension in fresh LB broth was used to start the culture on LB agar plates. Subsequently, the MMPM bandages were gently placed on the culture plate, and SERS measurements were performed at various time intervals with 0.4 mW and 5 s integration time. For determining the viable bacteria, bacteria were scraped off the MMPM and LB agar in 1 mL phosphate-buffered saline using an inoculating loop, followed by sonication. The bacterial suspension was serially diluted in LB and placed onto LB agar plates. The CFUs were counted after 48 h to obtain the concentration.

Multivariate Analysis: Cosmic Ray removal and background subtraction were performed using the Project v4.1 Software (WITec, Germany). Subsequently, ERS calibration and data truncation were performed in MATLAB. PCA and LDA were performed using R software.

Supporting Information

Supporting Information is available from the Wiley Online Library or from the author.

Acknowledgements

This work was supported by US AFOSR Young Investigator Award FA9550-18-1-0328 and US AFOSR DURIP Award FA9550-19-1-0287. This work was also supported by the US National Science Foundation grants: OISE-1545756, CBET-2029911, and DMR-2139317. Laboratory and instrumentation support was provided by NanoEarth—a node of the NSF-supported NNCI (NSF award number #1542100). Additional support was provided by the Sustainable Nanotechnology Interdisciplinary Graduate Program (VTSuN IGEP), funded by the Virginia Tech.

Conflict of Interest

The authors declare no conflict of interest.

Data Availability Statement

The data that support the findings of this study are available from the corresponding author upon reasonable request.

Keywords

bacterial biofilms, mesh devices, multiresonant plasmonics, nanoimprint lithography, nonlinear plasmonics, surface-enhanced Raman spectroscopy

Received: November 9, 2021
Revised: January 30, 2022
Published online: February 27, 2022

---

[1] a) H. Li, H. Liu, M. Sun, Y. Huang, L. Xu, *Adv. Mater.* **2021**, *33*, 2004425; b) S. Bose, M. Roy, A. Bandyopadhyay, *Trends Biotechnol.* **2012**, *30*, 546; c) Q. L. Loh, C. Choong, *Tissue Eng., Part B* **2013**, *19*, 485.

[2] a) A. Kalmykov, C. Huang, J. Bliley, D. Shiwarski, J. Tashman, A. Abdullah, S. K. Rastogi, S. Shukla, E. Mataev, A. W. Feinberg, *Sci. Adv.* **2019**, *5*, eaax0729; b) M. McDonald, D. Sebinger, L. Brauns, L. Gonzalez-Cano, Y. Menuchin-Lasowski, M. Mierzejewski, O.-E. Psathaki, A. Stumpf, J. Wickham, T. Rauen, bioRxiv 2021, 2020.09. 02.279125.

[3] B. Tian, J. Liu, T. Dvir, L. Jin, J. H. Tsui, Q. Qing, Z. Suo, R. Langer, D. S. Kohane, C. M. Lieber, *Nat. Mater.* **2012**, *11*, 986.

[4] a) A. Miyamoto, S. Lee, N. F. Cooray, S. Lee, M. Mori, N. Matsuhisa, H. Jin, L. Yoda, T. Yokota, A. Itoh, *Nat. Nanotechnol.* **2017**, *12*, 907; b) W. Zhou, S. Yao, H. Wang, Q. Du, Y. Ma, Y. Zhu, *ACS Nano* **2020**, *14*, 5798.

[5] a) X. Dai, W. Zhou, T. Gao, J. Liu, C. M. Lieber, *Nat. Nanotechnol.* **2016**, *11*, 776;/bib> b) Q. Li, K. Nan, P. L.e Floch, Z. Lin, H. Sheng, T. S. Blum, J. Liu, *Nano Lett.* **2019**, *19*, 5781.

[6] J. Liu, T.-M. Fu, Z. Cheng, G. Hong, T. Zhou, L. Jin, M. Duvvuri, Z. Jiang, P. Kruskal, C. Xie, Z. Suo, Y. Fang, C. M. Lieber, *Nat. Nanotechnol.* **2015**, *10*, 629.

[7] T. Zhou, G. Hong, T.-M. Fu, X. Yang, T. G. Schuhmann, R. D. Viveros, C. M. Lieber, *Proc. Natl. Acad. Sci. U. S. A.* **2017**, *114*, 5894.

[8] J. A. Schuller, E. S. Barnard, W. Cai, Y. C. Jun, J. S. White, M. L. Brongersma, *Nat. Mater.* **2010**, *9*, 193.

[9] a) L. Novotny, N. Van Hulst, *Nat. Photonics* **2011**, *5*, 83; b) J. N. Anker, W. P. Hall, O. Lyandres, N. C. Shah, J. Zhao, R. P. Van Duyne, *Nat. Mater.* **2008**, *7*, 442; c) S.-Y. Ding, J. Yi, J.-F. Li, B. Ren, D.-Y. Wu, R. Panneerselvam, Z.-Q. Tian, *Nat. Rev. Mater.* **2016**, *1*, 16021; d) M. L. Brongersma, N. J. Halas, P. Nordlander, *Nat. Nanotechnol.* **2015**, *10*, 25.

[10] a) C. Zong, M. Xu, L.-J. Xu, T. Wei, X. Ma, X.-S. Zheng, R. Hu, B. Ren, *Chem. Rev.* **2018**, *118*, 4946; b) J. Langer, D. Jimenez de Aberasturi, J. Aizpurua, R. A. Alvarez-Puebla, B. Auguié, J. J. Baumberg, G. C. Bazan, S. E. Bell, A. Boisen, A. G. Brolo, *ACS Nano* **2019**, *14*, 28.

[11] a) G. Kuku, M. Altunbek, M. Culha, *Anal. Chem.* **2017**, *89*, 11160; b) X.-S. Zheng, I. J. Jahn, K. Weber, D. Cialla-May, J. Popp, *Spectrochim. Acta, Part A* **2018**, *197*, 56; c) W. Nam, X. Ren, S. A. S. Tali, P. Ghassemi, I. Kim, M. Agah, W. Zhou, *Nano Lett.* **2019**, *19*, 7273.

[12] a) M. Soler, C. S. Huertas, L. M. Lechuga, *Expert Rev. Mol. Diagn.* **2019**, *19*, 71; b) B. Špačková, P. Wrobel, M. Bocková, J. Homola, *Proc. IEEE* **2016**, *104*, 2380; c) J. Mejía-Salazar, O. N. Oliveira Jr., *Chem. Rev.* **2018**, *118*, 10617.

[13] a) J. Baumgart, L. Humbert, É. Boulais, R. Lachaine, J.-J. Lebrun, M. Meunier, *Biomaterials* **2012**, *33*, 2345; b) A. M. Wilson, J. Mazzaferri, É. Bergeron, S. Patskovsky, P. Marcoux-Valiquette, S. Costantino, P. Sapieha, M. Meunier, *Nano Lett.* **2018**, *18*, 6981.

[14] a) A. Mohanty, Q. Li, M. A. Tadayon, S. P. Roberts, G. R. Bhatt, E. Shim, X. Ji, J. Cardenas, S. A. Miller, A. Kepecs, M. Lipson, *Nat. Biomed. Eng.* **2020**, *4*, 223; b) J. L. Carvalho-de-Souza, J. S. Treger, B. Dang, S. B. Kent, D. R. Pepperberg, F. Bezanilla, *Neuron* **2015**, *86*, 207.

[15] S. A. S. Tali, W. Zhou, *Nanophotonics* **2019**, *8*, 1199.

[16] S. Fossati, S. Hageneder, S. Menad, E. Maillart, J. Dostalek, *Nanophotonics* **2020**, *9*, 3673.

[17] S. A. Safiabadi Tali, J. Song, W. Nam, W. Zhou, *Adv. Opt. Mater.* **2021**, *9*, 2001908.

[18] J. Butet, P.-F. Brevet, O. J. Martin, *ACS Nano* **2015**, *9*, 10545.

[19] a) G. Deka, C.-K. Sun, K. Fujita, S.-W. Chu, *Nanophotonics* **2017**, *6*, 31; b) W. R. Zipfel, R. M. Williams, W. W. Webb, *Nat. Biotechnol.* **2003**, *21*, 1369.

[20] a) H. Lee, Y. Lee, C. Song, H. R. Cho, R. Ghaffari, T. K. Choi, K. H. Kim, Y. B. Lee, D. Ling, H. Lee, S. J. Yu, S. H. Choi, T. Hyeon, D.-H. Kim, *Nat. Commun.* **2015**, *6*, 10059; b) M. K. Hosain, A. Kouzani, S. Tye, *Australas. Phys. Eng. Sci. Med.* **2014**, *37*, 619.

[21] a) M. Hentschel, M. Saliba, R. Vogelgesang, H. Giessen, A. P. Alivisatos, N. Liu, *Nano Lett.* **2010**, *10*, 2721; b) N. J. Halas, S. Lal, W.-S. Chang, S. Link, P. Nordlander, *Chem. Rev.* **2011**, *111*, 3913; c) P. K. Jain, S. Eustis, M. A. El-Sayed, *J. Phys. Chem. B* **2006**, *110*, 18243.

[22] a) O. Reshef, M. Saad-Bin-Alam, M. J. Huttunen, G. Carlow, B. T. Sullivan, J.-M. Ménard, K. Dolgaleva, R. W. Boyd, *Nano Lett.* **2019**, *19*, 6429; b) S. D. Gennaro, M. Rahmani, V. Giannini, H. Aouani, T. P. Sidiropoulos, M. Navarro-Cía, S. A. Maier, R. F. Oulton, *Nano Lett.* **2016**, *16*, 5278.

[23] K. Chen, G. Razinskas, H. Vieker, H. Gross, X. Wu, A. Beyer, A. Gölzhäuser, B. Hecht, *Nanoscale* **2018**, *10*, 17148.

[24] A. Leitis, M. L. Tseng, A. John-Herpin, Y. S. Kivshar, H. Altug, *Adv. Mater.* **2021**, *33*, 2102232.

[25] M. L. Tseng, Y.-W. Huang, M.-K. Hsiao, H. W. Huang, H. M. Chen, Y. L. Chen, C. H. Chu, N.-N. Chu, Y. J. He, C. M. Chang, *ACS Nano* **2012**, *6*, 5190.

[26] S. A. Safiabadi Tali, J. Song, W. Nam, W. Zhou, *Adv. Opt. Mater.* **2021**, *9*, 2001908.

[27] A. Axelevitch, B. Gorenstein, G. Golan, *Phys. Procedia* **2012**, *32*, 1.

[28] H. Cho, J. Kim, H. Park, J. Won Bang, M. Seop Hyun, Y. Bae, L. Ha, D. Yoon Kim, S. Min Kang, T. Jung Park, S. Seo, M. Choi, K.-Y. Suh, *Nat. Commun.* **2014**, *5*, 3137.

[29] J. W. Jeong, S. R. Yang, Y. H. Hur, S. W. Kim, K. M. Baek, S. Yim, H.-I. Jang, J. H. Park, S. Y. Lee, C.-O. Park, Y. S. Jung, *Nat. Commun.* **2014**, *5*, 5387.

[30] A. Garg, W. Nam, W. Zhou, *ACS Appl. Mater. Interfaces* **2020**, *12*, 56290.

[31] J. Song, W. Nam, W. Zhou, *Adv. Mater. Technol.* **2019**, *4*, 1800689.

[32] J. Song, W. Zhou, *Nano Lett.* **2018**, *18*, 4409.
[33] J. Perumal, T. H. Yoon, H. S. Jang, J. J. Lee, D. P. Kim, *Nanotechnology* **2009**, *20*, 055704.
[34] a) A. Bouhelier, R. Bachelot, G. Lerondel, S. Kostcheev, P. Royer, G. Wiederrecht, *Phys. Rev. Lett.* **2005**, *95*, 267405; b) R. A. Farrer, F. L. Butterfield, V. W. Chen, J. T. Fourkas, *Nano Lett.* **2005**, *5*, 1139.
[35] a) N. Maccaferri, A. Zilli, T. Isoniemi, L. Ghirardini, M. Iarossi, M. Finazzi, M. Celebrano, F. De Angelis, *ACS Photonics* **2021**, *8*, 512; b) H. Hu, H. Duan, J. K. Yang, Z. X. Shen, *ACS Nano* **2012**, *6*, 10147; c) S. K. Andersen, A. Pors, S. I. Bozhevolnyi, *ACS Photonics* **2015**, *2*, 432.
[36] C. Hubert, L. Billot, P.-M. Adam, R. Bachelot, P. Royer, J. Grand, D. Gindre, K. Dorkenoo, A. Fort, *Appl. Phys. Lett.* **2007**, *90*, 181105.
[37] a) M. Lippitz, M. A. van Dijk, M. Orrit, *Nano Lett.* **2005**, *5*, 799; b) O. Schwartz, D. Oron, *Nano Lett.* **2009**, *9*, 4093.
[38] a) M. Kauranen, A. V. Zayats, *Nat. Photonics* **2012**, *6*, 737; b) J. Van Nieuwstadt, M. Sandtke, R. Harmsen, F. B. Segerink, J. Prangsma, S. Enoch, L. Kuipers, *Phys. Rev. Lett.* **2006**, *97*, 146102; c) S. Roke, M. Bonn, A. V. Petukhov, *Phys. Rev. B* **2004**, *70*, 115106.
[39] H.-D. Deng, G.-C. Li, Q.-F. Dai, M. Ouyang, S. Lan, V. A. Trofimov, T. M. Lysak, *Nanotechnology* **2013**, *24*, 075201.
[40] H. Im, K. C. Bantz, S. H. Lee, T. W. Johnson, C. L. Haynes, S. H. Oh, *Adv. Mater.* **2013**, *25*, 2678.
[41] W. Nam, Y. Zhao, J. Song, S. A. Safiabadi Tali, S. Kang, W. Zhu, H. J. Lezec, A. Agrawal, P. J. Vikesland, W. Zhou, *J. Phys. Chem. Lett.* **2020**, *11*, 9543.
[42] T. J. Beveridge, *J. Bacteriol.* **1999**, *181*, 4725.
[43] T.-T. Liu, Y.-H. Lin, C.-S. Hung, T.-J. Liu, Y. Chen, Y.-C. Huang, T.-H. Tsai, H.-H. Wang, D.-W. Wang, J.-K. Wang, Y.-L. Wang, C.-H. Lin, *PLoS One* **2009**, *4*, e5470.
[44] a) M. Allesen-Holm, K. B. Barken, L. Yang, M. Klausen, J. S. Webb, S. Kjelleberg, S. Molin, M. Givskov, T. Tolker-Nielsen, *Mol. Microbiol.* **2006**, *59*, 1114; b) H. Panlilio, C. V. Rice, *Biotechnol. Bioeng.* **2021**, *118*, 2129; c) C. B. Whitchurch, T. Tolker-Nielsen, P. C. Ragas, J. S. Mattick, *Science* **2002**, *295*, 1487.
[45] R. Pakkulnan, C. Anutrakunchai, S. Kanthawong, S. Taweechaisupapong, P. Chareonsudjai, S. Chareonsudjai, *PLoS One* **2019**, *14*, e0213288.
[46] a) H.-C. Flemming, J. Wingender, *Nat. Rev. Microbiol.* **2010**, *8*, 623; b) H.-C. Flemming, T. R. Neu, D. J. Wozniak, *J. Bacteriol.* **2007**, *189*, 7945.
[47] a) Y. Chao, T. Zhang, *Anal. Bioanal. Chem.* **2012**, *404*, 1465; b) S. Keleştemur, M. Çulha, *Appl. Spectrosc.* **2017**, *71*, 1180.
[48] a) N. N. Wickramasinghe, M. M. Hlaing, J. T. Ravensdale, R. Coorey, P. S. Chandry, G. A. Dykes, *Sci. Rep.* **2020**, *10*, 16457; b) W. Wang, S. Kang, P. J. Vikesland, *Environ. Sci. Technol.* **2021**, *55*, 9119.
[49] a) J. W. Costerton, Z. Lewandowski, D. E. Caldwell, D. R. Korber, H. M. Lappin-Scott, *Annu. Rev. Microbiol.* **1995**, *49*, 711; b) R. M. Donlan, *Emerging Infect. Dis.* **2002**, *8*, 881.
[50] F. L. Martin, J. G. Kelly, V. Llabjani, P. L. Martin-Hirsch, I. I. Patel, J. Trevisan, N. J. Fullwood, M. J. Walsh, *Nat. Protoc.* **2010**, *5*, 1748.
[51] J. G. Kelly, J. Trevisan, A. D. Scott, P. L. Carmichael, H. M. Pollock, P. L. Martin-Hirsch, F. L. Martin, *J. Proteome Res.* **2011**, *10*, 1437.